

1 Digital Elevation Model (DEM) uncertainty
2 and hazard analysis using a geophysical flow
3 model

4 E. R. Stefanescu¹, M. Bursik², G. Cordoba³, K. Dalbey⁴, M.
5 Jones⁵, A.K. Patra¹, D.C. Pieri⁶, E.B. Pitman¹, and M.F.
6 Sheridan²

7 ¹Department of Mechanical and Aerospace Engineering,
8 University at Buffalo

9 ²Department of Geology, University at Buffalo

10 ³Universidad de Nariño, Colombia

11 ⁴Sandia National Laboratories, Albuquerque, NM

12 ⁵Center for Computational Research, University at Buffalo

13 ⁶Jet Propulsion Laboratory, Caltech, Pasadena, CA, 91109
14 USA

15 December 4, 2011

16 **Abstract**

17 This paper describes a new methodology to quantify the variation
18 in the output of a computational fluid dynamics model for block and
19 ash flows, when the digital elevation model (DEM) of the terrain and
20 other inputs are given as a range of possible values with a prescribed

uncertainty. Integrating these variations in the possible flows as a function of input uncertainties provides us well-defined information on the hazards probability at specific locations, i.e., a hazard map. Earlier work provided a methodology for assessing hazards based on variations in flow initiation and friction parameters. This paper extends this to include the effect of terrain error and uncertainty. Our results based on potential flows at Mammoth Mountain, California, and Galeras Volcano, Colombia, establish the soundness of the approach and the effect of including the uncertainty in DEMs on the construction of probabilistic hazard maps.

1 Introduction

Perhaps the most fundamental product created by field volcanologists to characterize the potential for destruction of a volcano is the hazards map. Often a reasonable hazards map can be made when the distribution of deposits of a given type are well-exposed, and easily dated and mapped. In general, however, difficult logistics or paucity of previous work may render understanding of a volcano's history quite incomplete. Moreover, the depositional record on the flanks of a volcano cannot often be assumed to be very complete.

Several workers have thus explored the use of computational fluid dynamics (CFD) models to produce volcanic hazard maps for a variety of phenomena at a number of volcanoes (???). Hazard maps for ground-hugging flows that are constrained by the terrain, such as pyroclastic density currents and lava flows are often constructed using a digital representation of the terrain (??). Usually these terrain representations are digital elevation models (DEMs). For this type of study, terrain elevation is rightly recognized as the most essential and fundamental of variables in geographic analysis (?). In earlier work, (?) we introduced procedures for constructing hazard maps using ensembles of CFD models (the TITAN2D code (?)) of such flows constructed by establishing probability distributions of input uncertainties in

51 flow initiation (location and volumes) and sampling these. The important
52 contribution of DEM uncertainty to the variability of the flow outcomes was
53 not included in that work since there were no readily available procedures
54 for doing so. This work is focused on addressing this lacuna.

55 A digital representation of a terrain surface is an approximation of reality
56 and is often subject to significant error. The error is usually not known in
57 terms of both magnitude and spatial distribution. There are in fact large
58 uncertainties associated with the construction of DEMs. In (?) it was shown
59 that DEMs contain errors derived from a variety of sources: sampling, mea-
60 surement and interpolation, and these errors cannot always be well estimated.
61 When such DEMs are used in *a posteriori* analysis for instance in a CFD
62 model of possible flows the errors propagate to the predicted flow.

63 The most important part of DEM error propagation analysis is the ap-
64 propriate characterization of the error within the DEM itself, including in-
65 formation about its distribution and spatial structure (?). DEM vendors
66 generally provide users with a measure of vertical accuracy in the form of
67 the root mean squared error (RMSE) statistic. However many papers have
68 reported on the limitations of a single value of accuracy, stressing that DEM
69 error is spatially variable and autocorrelated (??). Also the magnitude of
70 the DEM error is closely related to the characteristics of the terrain surface.
71 For example, slope will influence interpolation procedures.

72 DEM error propagation analysis was introduced to the GIS community
73 in the early 1990s. In the work of ?, error propagation in calculating slope
74 and aspect was represented using Monte Carlo simulation and Taylor series
75 approximation. It was shown that standard deviations of slope and aspect
76 were higher than expected. The effect of error in the DEMs on the erosion
77 models was emphasized. A method used by ? in quantification of the un-
78 certainty of DEMs was to create various DEMs using different interpolation
79 methods and to examine the RMSE from the source map, sampling and mea-
80 surement error, and the interpolation process. It was concluded that RMSE
81 can be used as a general indicator of DEM uncertainty. In recent literature,

DEM error without spatial autocorrelation was considered to be a worst-case scenario (???), but no analysis based on terrain morphology and the effect of different DEMs was done. ? developed four different methods for representing the spatial dependence of error through random fields to assess the effect on topographic parameters of the DEM uncertainty. The study showed that uncertainty in the DEM is manifested at higher elevations in local steeper slopes, on both slope and elevation maps. ? showed that the effect of DEM uncertainty on the accuracy of slope and aspect estimation cannot be determined by using data from topographic maps or field surveys, because accurate derivatives cannot be determined.

One key feature of spatial data is the autocorrelation of observations in space. Generally, spatial autocorrelation refers to the correlation between the same attribute at two locations. Observations in close spatial proximity tend to be more related than are observations at larger distance or separation. Errors in spatial data (such as incorrect elevation values assigned to a point) are spatially autocorrelated. The effect of correlated DEM error has been investigated in the literature (??). It was shown that not only is error spatially variable throughout a DEM, but within the elevation model the error value of an individual grid cell is related to the error in neighboring cells. Unfortunately, DEM providers do not include information regarding the spatial dependence or spatial relationship of errors.

Stochastic modeling uses stochastic conditional simulation to generate multiple equally likely representations of an actual terrain surface. ?? computed a normal distribution of maps or realizations to reproduce the spatial autocorrelation encountered in the original error surface, filtered using a Gaussian convolution filter, with kernel sizes derived from autocorrelation analysis of the original error surfaces.

Various researchers have applied stochastic techniques to evaluate uncertainty in DEM data. ? stochastically simulated error in a DEM to evaluate the impact of DEM uncertainty on a least-cost-path application. ? investigated the effect of simulated changes in elevation at different levels of spatial

113 autocorrelation on slope and aspect calculations. ? produced uncertainty
114 surfaces to show the impact of DEM uncertainty on an ice sheet model. ?
115 developed a fuzzy framework to examine the probable and possible uncer-
116 tainties in classifying landslide hazard.

117 The aim of this paper is to quantify the variation in the output of a
118 computational flow model for block and ash flows, when the model inputs,
119 including the elevation values represented in the DEM, are uncertain or given
120 as a range of possible values. Integrating these variations in the possible flows
121 as a function of input uncertainties provides us well-defined information on
122 the probability of hazard at specific locations, i.e., a hazard map (?). In
123 particular, we focus on assessing the influence of DEM uncertainties (along
124 with uncertainties in initial size and location of the avalanche, and the in-
125 ternal and bed friction angles). There is uncertainty in all of these inputs,
126 which can be represented using either field data or stochastic methods. The
127 distribution or the range of the parameters can be obtained from laboratory
128 and field instruments for friction angles, and historical records of flow fre-
129 quency and magnitude for size of the initial failure. Stochastic methods are
130 used to assess the uncertainties in the DEMs: a perturbation of the elevation
131 based on the measured error model, and also an unconditional stochastic
132 simulation (?). Both methods generate multiple likely representations of the
133 actual terrain, while the second one accounts for the spatial autocorrelation
134 between elevation points. The effect of DEM uncertainty and its impact on
135 the model output is analyzed by constructing a hazards map and performing
136 a "probability analysis" for two volcanoes with different morphology: Galeras
137 Volcano, Colombia, and Mammoth Mountain, CA, USA. We adapt here an
138 approach based largely on the method of ?, which uses the difference between
139 two independent DEMs to train a Gaussian model of error.

140 We review in the next sections the basic methodology for generating an
141 ensemble of DEMs representative of the true DEM. Subsequent sections sum-
142 marize the TITAN2D flow simulation tool and its use in a systematic hazard
143 analysis. The hazards analysis tool itself uses ensembles of TITAN2D simu-

lations to construct statistical surrogate models of flow outcomes at different locations as a function of model inputs, such as flow volume, resistance to flow as modeled by a Coulomb frictional law, etc. Sampling of these surrogates leads to the construction of effective hazard maps that reflect the range of uncertainty in the model inputs.

2 Methodology

In previous work (?), the effect of DEM variability on the output of TITAN2D was investigated by comparing the output (maximum flow depth over the entire simulated time) from different DEMs of the same site. These DEMs were obtained from different techniques at different resolution. Two types of analysis were performed: a qualitative analysis and a statistical analysis. The qualitative analysis consisted of a comparison of the footprint of the flow, extended to a pixel based classification. The pixels were classified into inundated and non-inundated classes. For the statistical analysis we performed a Kolmogorov – Smirnov test to check if two output datasets differed significantly. The conclusion was that for moderate and smaller scale flows, use of different DEMs affects computation of accurate footprints of the flow.

This conclusion motivated us in examining the effect of DEM uncertainty by creating a model of the error and sampling it to create an ensemble of possible terrains. The flow simulation is then run on every member of this ensemble.

Naive, cell-by-cell approaches to treating DEM uncertainty quickly lead to the use of thousands if not millions of random variables, resulting in a computationally infeasible problem. On the other hand, the error model described above can be parameterized with one or two random variables. The parametrization methods are based on the assumption that the available DEM is a representation of the terrain to which errors have been added because of instrumental uncertainty. Therefore, the DEM can be assumed

173 to be one of an infinite number of elevation realizations.

174 **2.1 Method 1**

In this paper, we have available two "types" of DEMs of each mountain, which are used in creating DEM-to-DEM difference maps. Different realizations of the terrain were constructed by adding to one DEM – considered to represent the "true" elevation – a "random" perturbation. Since any two types of DEMs are obtained using different techniques, the difference between them can be added to that which is assumed to be the "true" DEM to give us a set of possible DEMs. Thus, the resulting realizations are consistent with the available set of DEMs. Randomness in the perturbations is created by multiplying the difference map with a normally distributed factor between 0 and 1.

$$R = M + \epsilon \cdot \text{Diff} \quad (1)$$

175 where R is a realization of the terrain, M is the DEM that best represents
176 the terrain (the "true" DEM), Diff is the difference map and ϵ is a random
177 variable. In this way we can define a set of DEM realizations using only one
178 random variable.

179 **2.2 Method 2**

For elevation, data at any grid point in a DEM tends to be related to data from nearby points. This is the principal motivation of Method 2, based on the work of (?). If more than one DEM exists for the same location, then difference maps can be constructed. Such maps are termed error maps. These maps are spatially autocorrelated. Random fields can be used to represent these spatially autocorrelated data points. Let $Z(\mathcal{U})$ be a continuous random field used to characterize unknown elevation errors (differences). The random field function we use is implemented in the function *r.random.surface* (?) of GRASS GIS (?), and generates fields obtained using a normal distribution (mean of 0.0 and variance of 1.0). The random field function derives its

spatial dependence from the use of a distance based decay filter function. The following equation is used to generate the random field:

$$Z(\mathcal{U}) = \frac{\sum_v w_{u,v} \epsilon_v}{\sqrt{\sum_v w_{u,v}^2}}, \quad u \in \mathcal{U}, v \in \mathcal{V} \quad (2)$$

$$w_{u,v} = \begin{cases} 1 & : d_{u,v} \leq F \\ \left(1 - \frac{d_{u,v}-F}{D-F}\right)^E & F < d_{u,v} \leq D, u \in \mathcal{U}, v \in \mathcal{V} \\ 0 & : d_{u,v} > D \end{cases} \quad (3)$$

180 where \mathcal{V} is the set of points potentially influencing points in a given area, \mathcal{U} ,
 181 $w_{u,v}$ is the spatial autocorrelative effect between points $u \in \mathcal{U}$ and $v \in \mathcal{V}$, ϵ_v
 182 is a random variable with a mean of 0 and variance of 1, $d_{u,v}$ is the distance
 183 between u and v , D is the minimum distance of spatial independence, E is the
 184 distance decay exponent, and F the distance at which errors are completely
 185 correlated.

186 A set of random fields is calibrated to the spatial variation of the field
 187 being simulated using a correlogram function. We do this by fitting the cor-
 188 relogram and choosing the best descriptive parameters of the random field
 189 (the minimum distance of spatial independence, the correlated distance de-
 190 cay exponent and the filter parameter) in a weighted least-square estimator
 191 implemented in GRASS's *r.lags.difference*. After running hundreds of tests
 192 with multiple combinations of D , E and F , we found the best random field to
 193 fit the error map characteristics based on the minimum sum of least squares
 194 difference between an error field's correlogram and the target correlogram.
 195 Figure ?? shows a sample error map correlogram and several trial correlo-
 196 grams closely fitting it. From Eqn ?? it can be seen that the parameters
 197 D , E and F influence the shape/look of the correlogram. We note that the
 198 main impact of the exponent value is to determining the roughness of the
 199 texture of the random surface. Texture roughness will decrease as the ex-
 200 ponent value gets closer to 1.0. Once the parameters are set to a certain
 201 value as determined above we are able to sample from a normal distribution

202 values for ϵ_v as given in Eqn ?? to generate a possible perturbation of the
 203 provided DEMs. In this way a normal distribution of possible terrain maps
 204 is produced where the mean of the distribution represents the original DEM
 205 used as the “true” surface.

The correlogram model was used with sequential Gaussian simulation to generate N error map realizations. Each error realization was added to the “true” DEM to generate equally probable realizations of the topography for the error structure of a DEM under consideration:

$$R(U) = m(U) + m(m(T)) + (m(s^2(T)) \cdot \epsilon) \cdot Z(U) \quad (4)$$

206 where $R(U)$ is a realization of an elevation dataset $m(U)$, T is a group of sets
 207 of spatially uncorrelated sample points, and ϵ is a random variable with mean
 208 0.0 and variance 1.0. The mean and the standard deviation are determined
 209 from randomly drawn, spatially independent points scattered across the error
 210 map. The error map was generated by subtracting the lower quality DEM
 211 from the “true” DEM, and characterizes the error of the lower quality DEM
 212 at each point.

213 2.3 DEM realizations

214 Many DEM users are aware that DEM uncertainty affects the results of
 215 their application, however, in most cases the DEM is accepted as the true
 216 representation of the earth’s surface. In this section, the two methods for
 217 generating multiple realizations of the terrain are presented for both Galeras
 218 Volcano and Mammoth Mountain, to test whether it is safe to assume that
 219 the representation of topography is acceptable as it is.

220 The motivation for creating realizations of the DEM was to be able to use
 221 the DEM along with other uncertain parameters as uncertain inputs for the
 222 calculation of a hazard map using the computational fluid dynamical model
 223 TITAN2D. One of our working hypotheses is that the DEM contributes a
 224 significant proportion of the variance in simulated flow, hence hazard map

225 output. For sampling the input parameter space, a Latin Hypercube Sam-
226 pling (LHS) was implemented.

227 For Galeras Volcano, two test DEMs at 30 m spacing were considered for
228 our analysis. The SRTM (Shuttle Radar Topography Mission) 30m DEM
229 was derived by spline interpolation from a 90m DEM of southern Colombia
230 using radar data collected in 2000, while the ASTER (Advanced Spaceborne
231 Thermal Emission and Reflection Radiometer) DEM was calculated at the
232 Jet Propulsion Laboratory using orthorectified imagery from 12 January 2010
233 (Fig. ?? a). The ASTER dataset was used as a surrogate for the “true”
234 elevation while the SRTM dataset was used in creating the error model.

235 Two 30-m resolution DEMs derived from independent techniques were
236 used for Mammoth Mountain. A TOPSAR dataset was considered to be the
237 “true” elevation, while an SRTM dataset was used in creating the error map.
238 A rectangular area of approximately 42 kilometers² was defined within the
239 TOPSAR and SRTM DEMs (Fig. ?? b).

240 For Method 1, sixty-four (64) DEM realizations were created and used as
241 input parameters for the TITAN2D simulator along with uncertain parame-
242 ters presented in ???. The input space is defined by seven parameters.

243 As described above for Method 2, realizations of the terrain surface were
244 created by taking into consideration the spatial autocorrelation of the error.
245 The error map was obtained by subtracting the elevation of a given DEM
246 from the “true” elevation at each location. The correlogram for the difference
247 map was calculated to determine the range of spatial dependence of eleva-
248 tion points. We found that spatial dependence persisted above a threshold
249 value of the correlogram cross-correlation coefficient of 0.4 to a distance of
250 2500 meters for Galeras and 2100 meters for Mammoth. To determine the
251 probability distribution function (pdf) for the stochastic simulation, 91 sets
252 of spot locations were selected from the map, each set containing 91 points,
253 all pairs of points were separated by more than 2500 meters or 2100 meters,
254 respectively. For each DEM, pdf statistics were derived. The random field
255 parameters were chosen after testing more than 400 random field parameters

for the smallest difference between the error model correlogram and the random field. This occurs when the minimum distance of spatial independence, $D = 2500$; the distance decay, $E = 0.8$, and the filter parameter, $F = 400$ for Galeras and $D = 2100$, $E = 0.7$, and $F = 350$ for Mammoth. A total of 64 equally probable potential elevation surfaces of the area having a 30-m resolution were generated.

2.4 Hazard map construction

There are numerous ways to create a volcanic hazard map based on computational fluid dynamics modeling. The traditional Monte Carlo method can be used if we assume that uncertainty in model input parameters is the main restriction to our knowledge of future events at a given volcano. This is the case, for example, if we know that block and ash flows are common at a given volcano, but it is difficult to know the size or volume of potential future events. Although Monte Carlo is relatively simple to implement, it converges slowly and is unaffordable computationally because of the number of time-consuming simulations. A single TITAN2D run might take 20 minutes on a single processor. To obtain three-digit accuracy in the expected value of a specified function would require a million runs. One million runs of 20-min calculations running non-stop on 64 processor would take 217 days (?).

Here, we briefly described the use of an hierarchical emulator that significantly reduces computational cost; a detailed discussion of the methodology can be found in ???. An emulator can be thought of as a fast surrogate for a single numerical model simulation (a simulator). We describe the process of computing a hazard map for block and ash flows with uncertain model inputs introduced by ?. Two-level construction of a group or ensemble of emulators is used to include a separation of uncertain inputs and geographic coordinates. The process starts by identifying the model inputs whose uncertainties will drive the process. In our case, the uncertain flow inputs we use are volume and shape, starting location, basal and internal friction angles, and

286 finally topography, as given by the DEM. For the resulting eight-dimensional
 287 parameter input space, a Latin Hypercube Sampling was performed to deter-
 288 mine parameter values at which simulations were to be run (?). As priors for
 289 the emulator, simulation outputs for each of these input parameter vectors
 290 were stored at 64 grid points.

291 The output variable of interest for our application is the field of maximum
 292 flow depth over time for each spatial position, at each of the downsampled
 293 input parameter gridpoints. Tessellations of the geographic coordinate space
 294 and the parameter input space are constructed (we use Delaunay triangulation).
 295 At a designated location, \mathbf{x}^* , of the input parameter plus spatial
 296 coordinate space at which the hazard is to be computed, the covering simplex
 297 $S_{\mathbf{x}}^*$ of the parameter space is identified, and all nodes of that simplex
 298 are enumerated, as are all nodes within a neighborhood (two hops in the
 299 tessellation) of the covering simplex nodes. For each such two-hop node, we
 300 tessellate in the spatial coordinates and evaluate all emulators constructed
 301 over these nodes. We average these coordinate space emulators to (the coordinate
 302 components of) \mathbf{x}^* by barycentric weighting; notice there will be an
 303 emulator for each parameter input sample point. Now in the input parameter
 304 space, construct a tessellation of the two-hop nodes and average the emulators
 305 to \mathbf{x}^* by barycentric weighting of the fine-scale emulator. The emulator
 306 is now readily and quickly evaluated for each evaluation. The hazard map
 307 construction can now proceed by treating the emulator as a surrogate for
 308 the simulator in the classical Monte Carlo procedure. For any point in the
 309 domain we can now exercise the emulator to get potential flows and hence
 310 exceedance probabilities.

311 2.5 TITAN2D and flow simulations

312 TITAN2D was developed for modeling dry geophysical granular flows, such
 313 as debris avalanches and block and ash flows. Given a digital elevation map
 314 specifying the topography of a volcano and the values of input parameters,
 315 including the initial volume of erupted material and the friction angles, TI-

316 TAN2D calculates the flow depth and velocity at any location throughout
 317 the duration of an event. The TITAN2D code combines numerical simu-
 318 lations of a natural granular flow with digital terrain data. It is based on
 319 a depth-averaged model for an incompressible granular materia governed by
 320 Coulomb-type friction interactions (?). The governing equations are obtained
 321 by applying conservation laws to the incompressible continuum, providing
 322 appropriate constitutive modeling assumptions, and then taking advantage
 323 of the shallowness of the flows (flows are much longer and wider than they
 324 are deep) to obtain simpler depth-averaged representations (?). The mo-
 325 tion of the material is considered to be gravitationally driven and resisted
 326 by both internal and bed friction. The stress boundary conditions are: no
 327 stress at the upper free-surface and a Coulomb-like friction law imposed at
 328 the interface between the material and the basal surface.

329 The primary factor driving the flow is the component of gravity tangential
 330 to the surface, which depends on a local slope computed from the elevation
 331 data, hence, the criticality of the DEM to the flow computations. The result-
 332 ing hyperbolic system of equations was solved using a finite-volume scheme
 333 with a second-order Godunov solver. Although many real geophysical flows
 334 — such as debris flows — are fluidized, in this study we deal only with gran-
 335 ular material that has not been fluidized, such as dome-collapse block and
 336 ash flows or rock avalanches initiated by slope instability. The program runs
 337 in parallel, using the Message Passing Interface (MPI) to allow communica-
 338 tion between multiple processors, increasing computational power, decreasing
 339 computational time and allowing use of large datasets. The algorithm uses
 340 local adaptive mesh refinement for shock capturing, and dynamic load bal-
 341 ancing for the efficient use of computational resources. Topographic data
 342 are included in the simulation through a preprocessing routine in which the
 343 digital elevation data are imported. TITAN2D performs flow simulations on
 344 a DEM of a desired region, the simulation accuracy being highly dependent
 345 on the level of the DEM resolution and quality.

346 Inputs to the code are the size and location of the initial volume, the

internal and bed friction and the DEM. ? presented several methods for characterizing the effect of input data uncertainty on model output. At that time, efficient methods for representing the uncertainty associated with spatial parameters like terrain elevation were not well understood.

2.6 Bayes Linear Method

The straightforward way to account for uncertain inputs and stochastic forcing is a Monte Carlo approach — run many simulations and ‘average’ the results in some fashion. If simulations are expensive to run, this approach is not feasible. To circumvent this difficulty, the statistics community has developed the idea of an emulator. In essence, the emulator is a regression surface based on a representative sample of simulations at selected inputs, accompanied by statistical error bounds. Equipped with this surface, output values at new (untested) input values need not be run. Instead output results can be determined by evaluating the emulator. There are indeed many methods — kriging, metamodels, support vector machines, etc., by which such surrogates may be constructed and there exists a body of literature on the topic (??). One often-used emulator is the GAuSSian Process (GASP) emulator, which assumes the regression has the form of a trend plus a Gaussian (????). To construct a GASP emulator, the covariance structure of the Gaussian must be assumed and parameters determined by Bayesian or partially Bayesian methodology. A fully Bayesian determination of the emulator can be costly, especially if the input data is high-dimensional. Here we use the Bayes Linear method (BLM) (?) to construct an emulator. Given prior beliefs (B) of mean and variance, the BLM updates these beliefs conditioned on the data (D). Note that “data” generally here refers to the output of computationally expensive physics based simulators. Because only the first two moments of a distribution are determined, the BLM is exact only for Gaussian distributions. As an emulator construction, the BLM update is simpler than a full GASP construction, but the resulting emulator is comparable. Given the

376 prior expectation $E[B]$ and variance $var(B)$, the BLM updates are

$$\begin{aligned} E_D(B) &= E[B] + cov(B, D)(var(D))^{-1}[D - E[D]] \\ var_D(B) &= var(B) - cov(B, D)(var(D))^{-1}cov(D, B) \end{aligned} \quad (5)$$

377 These update formulae can be derived by minimizing the mean square error
 378 $(B - a^T D)^2$ between B and some linear combination of the data. Thus the
 379 BLM update can be viewed as the projection of the set of prior beliefs onto
 380 the span of the data.

381 **3 Implementation**

382 **3.1 Case study I: Galeras Volcano**

383 Galeras Volcano (elevation 4,276 meters), located in southwestern Colombia
 384 ($1^\circ 13.31' N$ and $77^\circ 21.68' W$), is one of the most active volcanoes on the world
 385 (?). Nearly 400,000 people currently live near the volcano; 10,000 of them
 386 reside within the zone of high volcanic hazard. Pyroclastic flows pose a major
 387 hazard for this population. The current period of activity that began in 2004
 388 presents a serious problem for all stakeholders: decision makers, scientists,
 389 public safety officials, and the general population. Computational modeling
 390 has the potential to provide useful information for hazard assessment and risk
 391 mitigation. However, there is a need to evaluate the validity of the modeling
 392 and the quality of the DEMs available for use in such modeling.

393 Galeras is an important volcano for computational flow modeling from
 394 both risk management and scientific perspectives (?). Forecasts of volcanic
 395 explosions using various geophysical tools (?) have occasionally brought
 396 public warnings to a high level of alert during the past 20 years. When the
 397 alert reaches the highest level, the public are urged to evacuate some local
 398 areas; this occurred as recently as January, 2010. The worst event at Galeras
 399 occurred in 1993, when an eruption killed 9 scientists and journalists (?).

400 The topography of the volcano presents a problem for creation of a good
 401 DEM. The irregular morphology on a small scale, with steep slopes, narrow

channels, deep gorges and abrupt cliffs poses problems for the creation of accurate topographic models (?). In addition, the current flow hazard map at Galeras is mainly based on the sparse geological record (?). Dense vegetation, deep erosion, successive deposits of lava and pyroclastic flows hinder the tracing of specific deposits in the field. The diverse effects of this landscape, as reflected in DEMs created by different processes and of different scales, must be examined and quantified to determine the level of confidence that can be placed in model results. Galeras provides a wide range of topographic features that challenge the use of computational flow models.

3.2 Case study II : Mammoth Mountain

Mammoth Mountain is a large, geologically young, composite dome volcano located on the southwestern rim of Long Valley Caldera, California (?). There are many active hazards issues for Mammoth Mountain, including snow avalanches, rock avalanches and debris flows. In addition, it is intersected by the Mono-Inyo Craters volcanic chain, which is the most active volcanic region in the southwestern U.S. If Mono-Inyo type activity occurs on Mammoth Mountain, then domes may form. These new domes would be growing atop a steep edifice, and therefore could become gravitationally unstable. Given that block and ash flows occurred at Mammoth Mountain during its older dome growth stage, there is reason to believe that renewed dome formation would result in block and ash flow activity. If this is so, then parts of Mammoth Lakes, CA, are at risk from block and ash flows. Our previous work on Mammoth Mountain (Stefanescu et al., submitted) was the testing of the hypothesis that different DEMs result in different model outputs of block and ash flow inundation.

3.3 Model Set-up

In our process to quantify the DEM uncertainties using TITAN2D, a set of parameters was drawn on which to set the bounds of the input domain: in-

430 ternal friction angle, basal friction angle, flow volume, location and DEM.
 431 The numerical values for these parameters were chosen to bracket the range
 432 of flow volumes and initial locations, and to be representative of the friction
 433 angles that have been used by other researchers in their computational mod-
 434 els. The same reasonable parameter values were used for both volcanoes,
 435 so they do not necessarily represent any optimization for a particular case.
 436 The internal friction angle has little effect on the output of the flow models
 437 (??). Many TITAN users have chosen values of internal friction that range
 438 between 15 and 37 degrees with values between 30 and 35 being the most
 439 frequent values used (??). For our study we use an internal friction angle
 440 uniformly distributed between 20 and 25 degrees.

441 The value of the basal friction angle has a large effect on flow dynamics in
 442 the TITAN2D simulations (??). Factors that could affect the choice of basal
 443 friction angle include the volume of the flow, the type of the pyroclastic flow,
 444 the nature of the substrate and the amount of channelization. ? listed the
 445 basal friction values chosen by TITAN2D users; they range between 5 and
 446 28 degrees; the mean value being about 15 degrees. We are using a basal
 447 friction angle uniformly distributed between 15 and 20 degrees.

448 Volumes of pyroclastic flows at stratovolcanoes typically cover a few or-
 449 ders of magnitude. The volume values in this study bracket the range of possi-
 450 ble pyroclastic flows for both Mammoth and Galeras. According to ?, Galeras
 451 volcano produced 5 large pyroclastic flow eruptive episodes; an historic erup-
 452 tion in 1866, and prehistoric events in 1100, 2300, 2900, and 4500 yBP. The
 453 total deposit volumes of these episodes range from $O(10^6 - 9 \times 10^6)m^3$. Block
 454 and ash flows on Mammoth Mountain might contain $O(10^5 - 10^7)m^3$ of ma-
 455 terial (??). Thus, our choice of volumes ranges from 1.9×10^5 to $5 \times 10^6 m^3$.
 456 The shape of the initial failure region is approximated as a paraboloid for
 457 which the volume is calculated as $V = \frac{\pi}{2} \cdot r_{min} \cdot r_{max} \cdot h_{max}$. For a good match
 458 of the volume range, the radius values were uniformly distributed between
 459 25 and 500 m, while the initial height followed the same distribution with
 460 values between 10 and 150 m.

Initiation locations were taken from previous mapping of vent sites, coupled with knowledge of known weak areas within the volcano as indicated by hydrothermal alteration. Around the centers of the separate initiation locations, different starting positions were uniformly distributed in a circle of radius 200 m. A rectangular area of approximative 40 km^2 was defined around the vent within the available DEMs as the potential run-out area.

4 Results and Conclusions

One of the goals of our analysis was to understand the effect of the spatial structure of available DEMs on hazard maps. Figure ?? (c) and (d) show the correlograms for the ASTER DEM and the TOPSAR DEM, which are the DEMs considered to best represent the real topography for Galeras Volcano and Mammoth Mountain, respectively. It is apparent that data processing resulted in a smoothing and filtering of the TOPSAR DEM which causes the correlation coefficient to vary smoothly as a function of distance and any two elevation values. Using a distance between two points of 2000m, for the ASTER DEM the correlation coefficient is 0.6, whereas for the TOPSAR DEM the correlation coefficient is 0.4. This means that elevation values within the ASTER DEM are more highly correlated.

Starting from these premises, we can explain the hazard map output for the cases when the DEM is considered to be an input parameter for the TITAND2D model. Figures ?? (a) and (c) display maps of Galeras of the probability that the flow depth will exceed 0.5 m in the next ten years using Method 1 or Method 2, respectively, to create the terrain realizations.

Figures ?? and ?? show maps at Galeras and Mammoth of the spatially varying lack of confidence in the probability hazard map depicted in Figure ?? (a) and (b), respectively. The lack of confidence is defined as the computed standard deviation of hazard probability σ_P divided by the hazard probability, P . When calculated by standard means, as was done here, the ratio σ_P/P measures the lack of confidence in the statistic, P , due to

490 insufficient re-sampling of the input parameter space.

491 After a visual inspection of the figures we can conclude that the difference
492 between hazard map outputs is more obvious for Galeras than for Mammoth
493 Mountain. From the lack of confidence figure it is observed that in both cases
494 the error is concentrated at flow margins.

495 For Mammoth Mountain the differences are less obvious, but with impor-
496 tant differences again concentrated at the edge of the flow. An illustration of
497 how the probabilities vary for Method 1 compared to Method 2 is shown in
498 Figure ???. We observe in comparing every point where there is a probability
499 of having a flow depth greater than 0.5 m, the results for Galeras show a
500 greater dispersion than do those for Mountain Mountain. When the flow is
501 deep, the probability is high and tends to cluster near unity for both moun-
502 tains. As the probability decreases, dispersion becomes greater for Galeras.
503 We can conclude that as the error map becomes more highly correlated, one
504 should use a more complex method for creation of topographic realizations
505 such as stochastic Method 2. It appears that the spatial autocorrelation of
506 the elevation points influences the hazard map output and a random pertur-
507 bation of the elevation such as that used in Method 1 will not capture this
508 effect.

509 One of the conclusions of our previous work was that for moderate and
510 smaller-sized flows, different representations of the terrain more profoundly
511 affect computation of an accurate flow footprint. For the present contribu-
512 tion, we have built a new set of hazard maps for the case when the volume is
513 low, with a range between $10^4 - 5 \times 10^4 \text{ m}^3$ and for a high volume between
514 $9 \times 10^6 - 5 \times 10^7 \text{ m}^3$. Since only 517 spatial cells for Mammoth and 872
515 cells for Galeras were included in the flow footprint for the low-volume case,
516 for any particular cell, the probability that the flow would include that cell
517 tends toward unity (in the case of cells within the starting region), or zero
518 (in the case of any cell outside of the starting region but still within the
519 footprint). Thus the probability plot appears nearly binary, which means
520 that we have a hazard (flow greater than 0.5m) with either probability ~ 1

521 or ~ 0 Figure ?? (a), (b). We observe that there is a significant mismatch
522 of prediction between the two methods (left upper corner and right lower
523 corner in both figures) for both volcanoes that can be critical in the case of
524 a hazards or risk assessment. For high-volume flows at Galeras, we observe
525 that the area of probability greater than zero is much smaller when we are
526 using Method 2 (topography is correlated) compared to Method 1 (no corre-
527 lation of error between topographic points). We do not know the reason for
528 this counterintuitive effect.

529 Our main goal was to explore the effect of DEM uncertainty in construct-
530 ing a hazards map. A quantitative and qualitative analysis is performed for
531 the case wherein the “original” or “best” deterministic DEM (ASTER 30m
532 for Galeras and TOPSAR 30m for Mammoth as in Figure ??) is used as
533 input parameter for the hierarchical emulator, the output of which is then
534 contrasted with the case wherein the input is a set of terrain realizations.

535 We thus compare the hazard maps produced when DEM uncertainty is
536 not included against maps produced when DEM uncertainty is included. Fig-
537 ures ?? and ?? show that for Galeras the probability that the flow was deeper
538 than 0.5m varies considerably from the case of no DEM uncertainty. Hence,
539 the DEM is an important input parameter of which the errors need to be
540 carefully considered in flow modeling, and the effect of the DEM is not dimin-
541 ished by other uncertain parameters or the methodology used. We observe
542 that the uncertainty of having flow greater than 0.5 m increases towards the
543 flow edge. For Mammoth Mountain, the DEM uncertainty results in more
544 uncertainty in the flow outline when Method 2 is used. One of the causes
545 might be that the flow propagates a shorter distance compared to that in the
546 original DEM.

547 Because the uncertainty in flow outline increases for the case of Galeras,
548 where the autocorrelation is higher, we can furthermore say that perturbing
549 the DEM is more important as autocorrelation increases.

550 **Acknowledgments.** This work was supported by NASA grant NNX08AF75G.
551 The work and opinions expressed herein are those of the authors alone and do
552 not reflect the opinion of NASA. We are grateful to JPL for the construction
553 and distribution of the TOPSAR dataset.

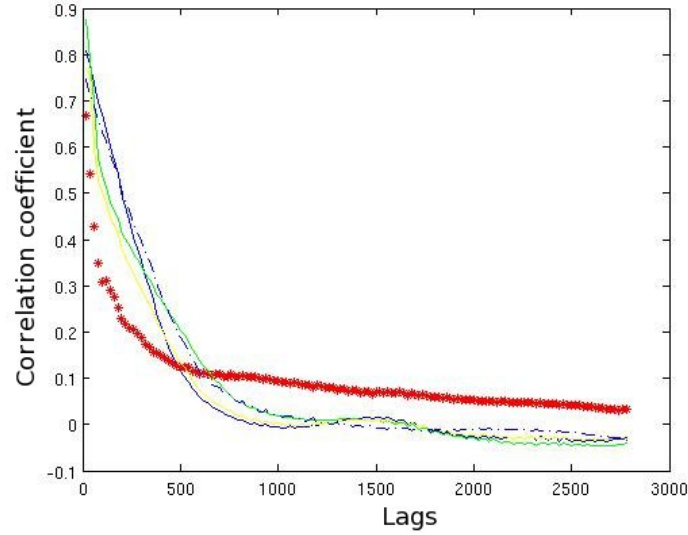
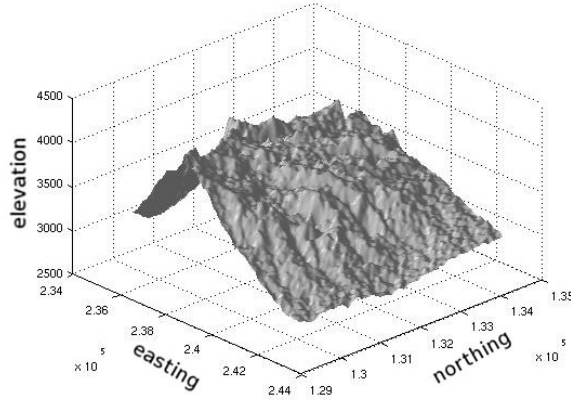
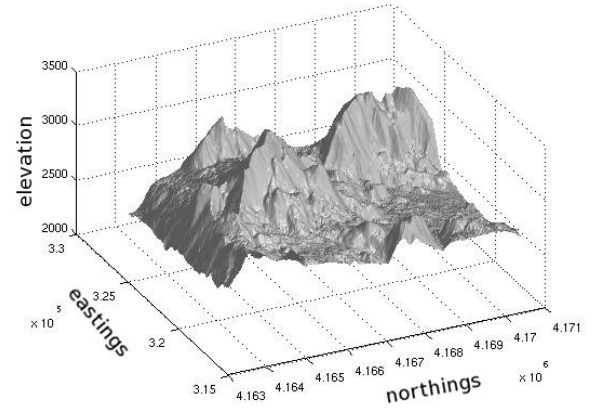


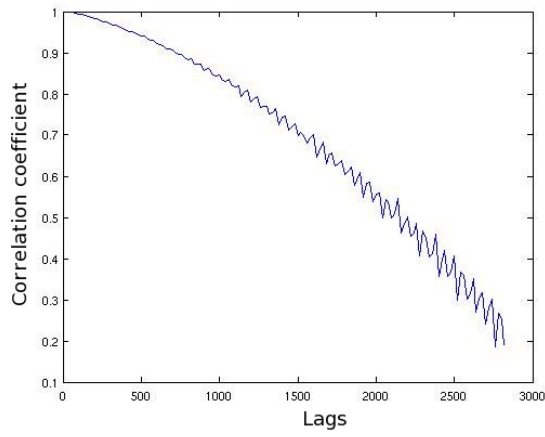
Figure 1: Error map correlogram (red) and various random fields fitted to this by choosing different values for the parameters D, E, F representing the distances of perfect correlation, decay exponent and spatial independence in Equation ??.



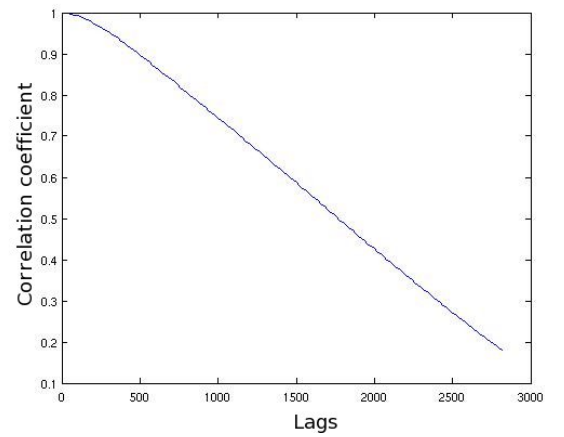
(a)



(b)



(c)



(d)

Figure 2: a) The Galeras ASTER 30m DEM terrain surface (Easting, Northing and elevation coordinates) (b) The Mammoth NED 30m DEM terrain surface (Easting Northing and elevation coordinates) (c) Galeras Volcano ASTER DEM correlogram (d) Mammoth Mountain TOPSAR DEM correlogram

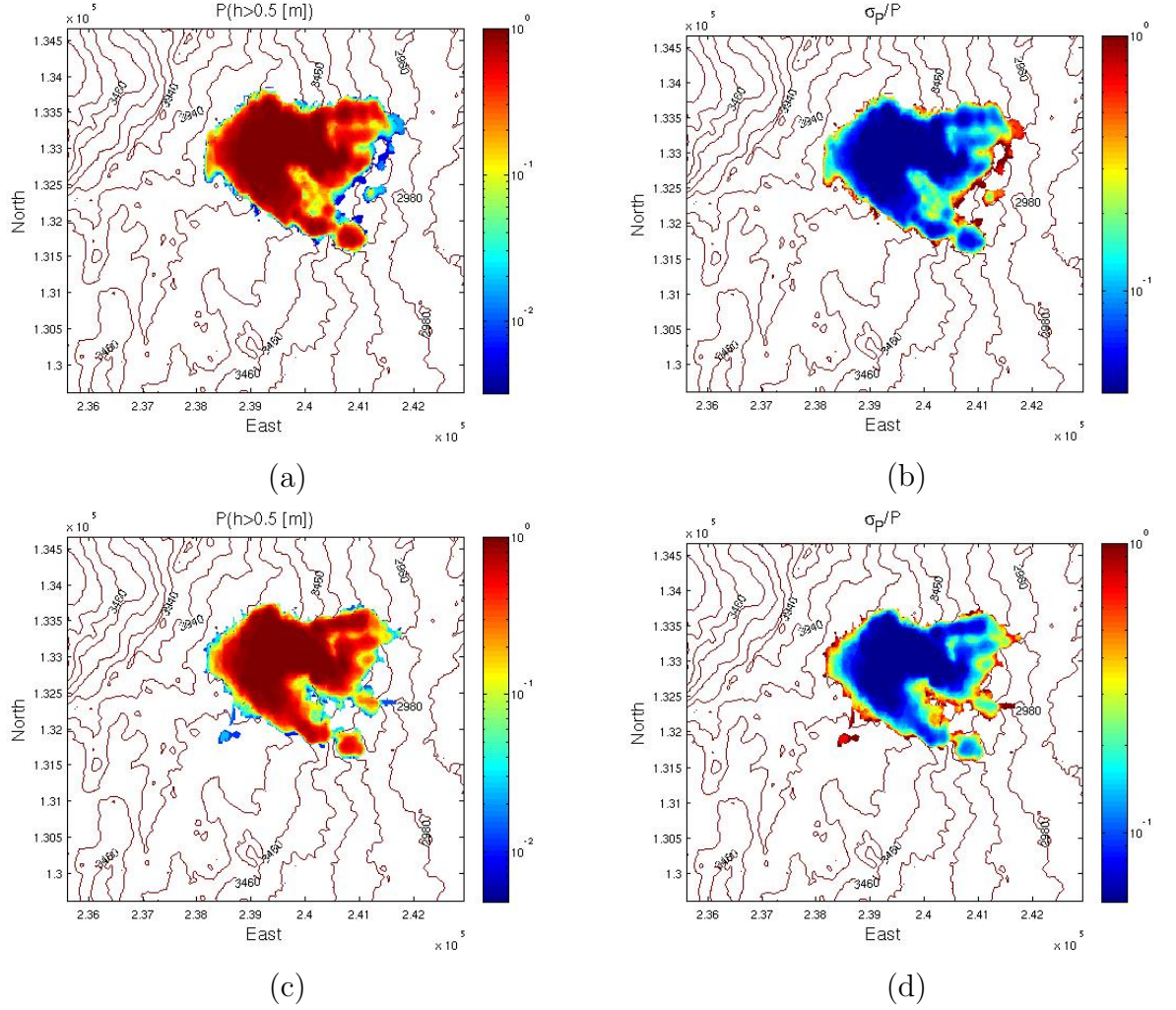


Figure 3: a) Probability that a flow will exceed 0.5 m in depth as a function of position on Galeras Volcano, Columbia, given the uncertainties in DEM and input parameters using Method 1 to create DEM realizations (b) Standard deviation in the estimate that the flow will exceed 0.5 m in depth – Method 1 (c) Probability that a flow will exceed 0.5 m in depth as a function of position on Galeras Volcano, Columbia, given the uncertainties in DEM and input parameters using Method 2 to create DEM realizations (d) Standard deviation in the estimate that the flow will exceed 0.5 m in depth – Method 2

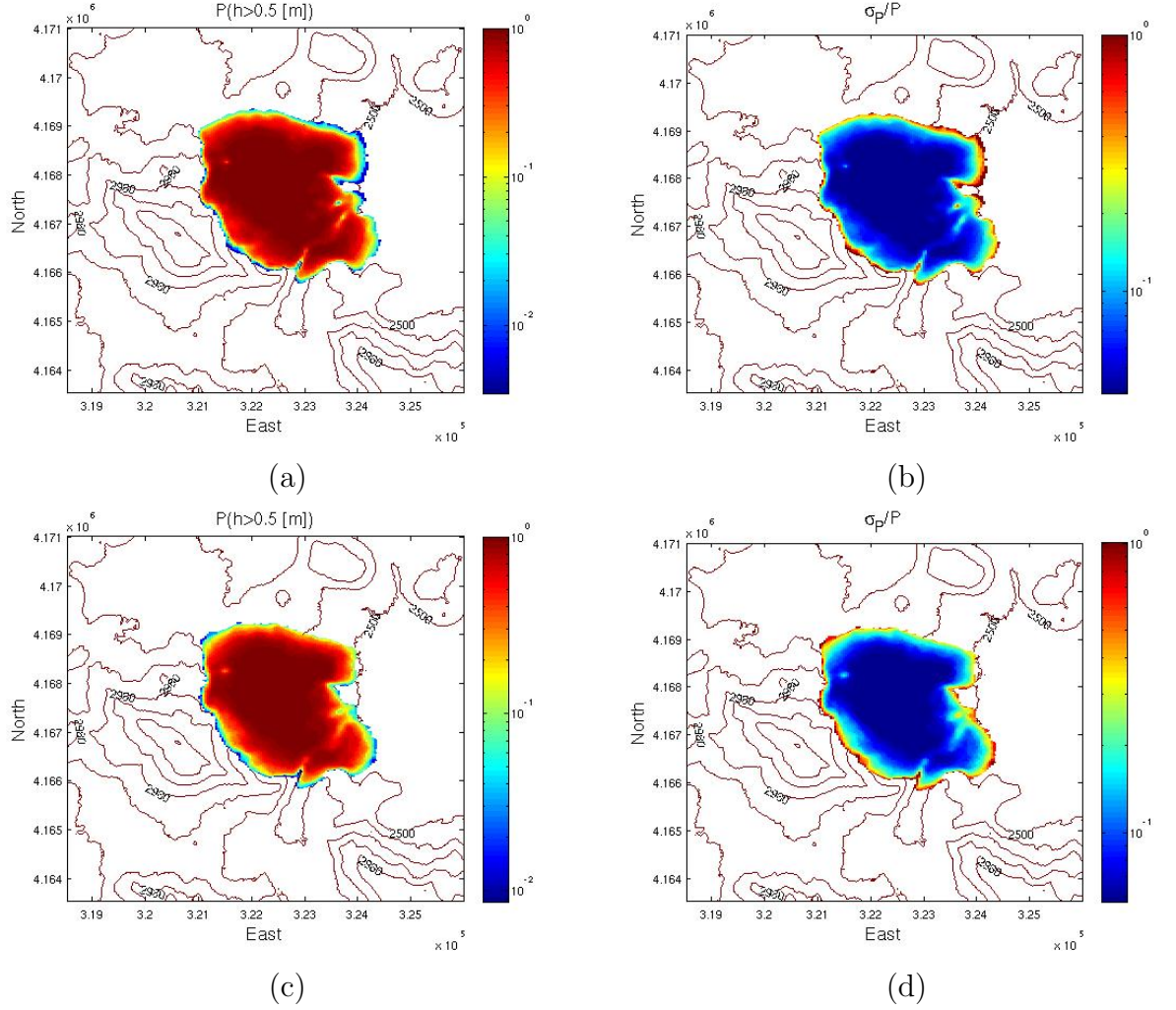
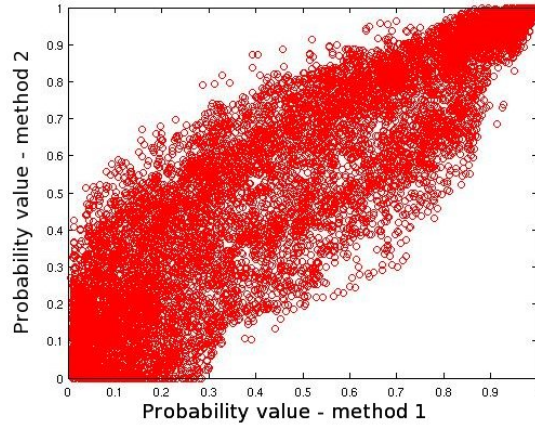
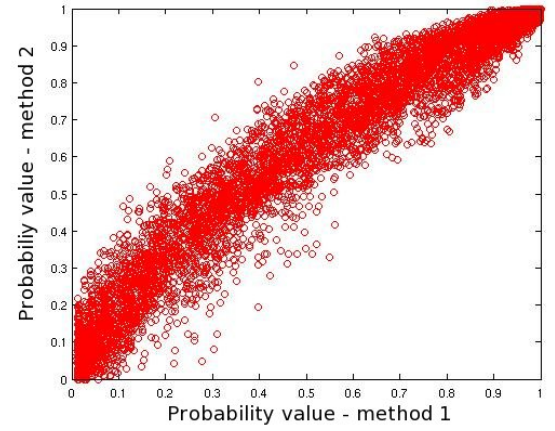


Figure 4: a) Probability that a flow will exceed 0.5 m in depth as a function of position on Mammoth Mountain, CA, given the uncertainties in DEM and input parameters using Method 1 to create DEM realizations. (b) Standard deviation in the estimate that the flow will exceed 0.5 m in depth – Method 1 (c) Probability that a flow will exceed 0.5 m in depth as a function of position on Mammoth Mountain, CA, given the uncertainties in DEM and input parameters using Method 2 to create DEM realizations. (b) Standard deviation in the estimate that the flow will exceed 0.5 m in depth – Method 2

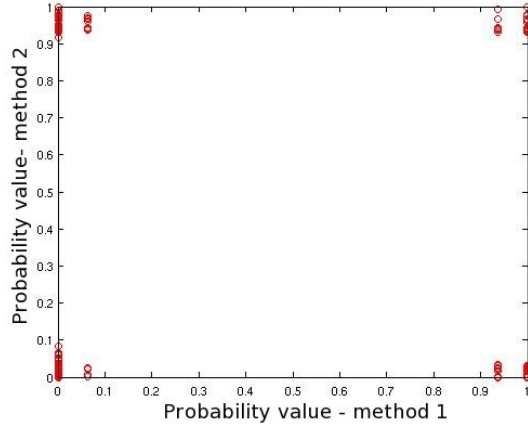


(a)

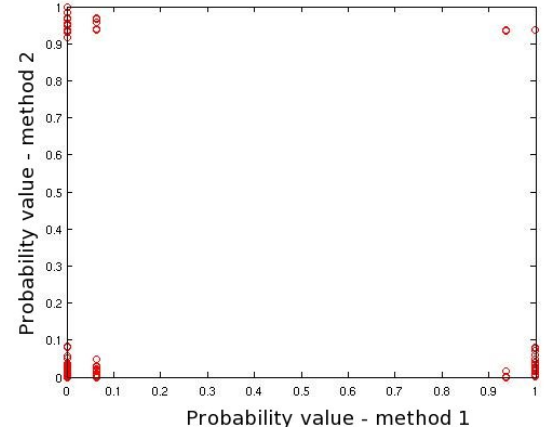


(b)

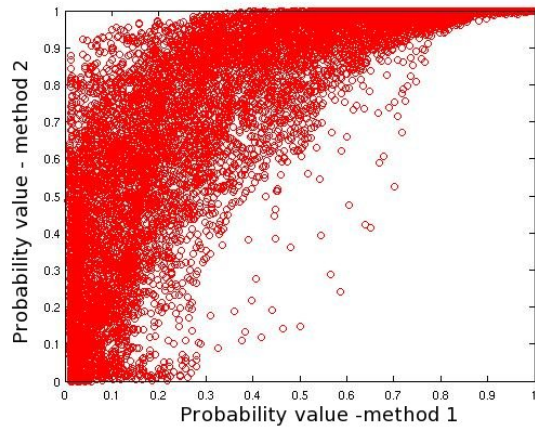
Figure 5: a) The probability that flow will exceed 0.5 m Method 1 versus Method 2 for Galeras Volcano, Colombia (b) The probability that flow will exceed 0.5 m Method 1 versus Method 2 for Mammoth Mountain, CA



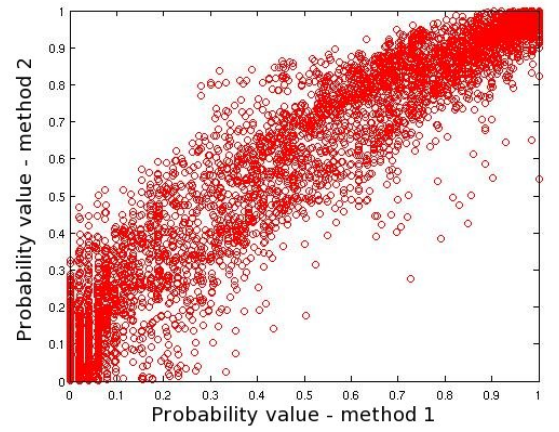
(a)



(b)



(c)



(d)

Figure 6: (a) The probability that flow will exceed 0.5 m Method 1 versus Method 2 for: (a) Galeras Volcano, Colombia for low flow (b) Mammoth Mountain, CA for low flow (c) Galeras Volcano, Colombia for high flow (d) Mammoth Mountain, CA for high flow

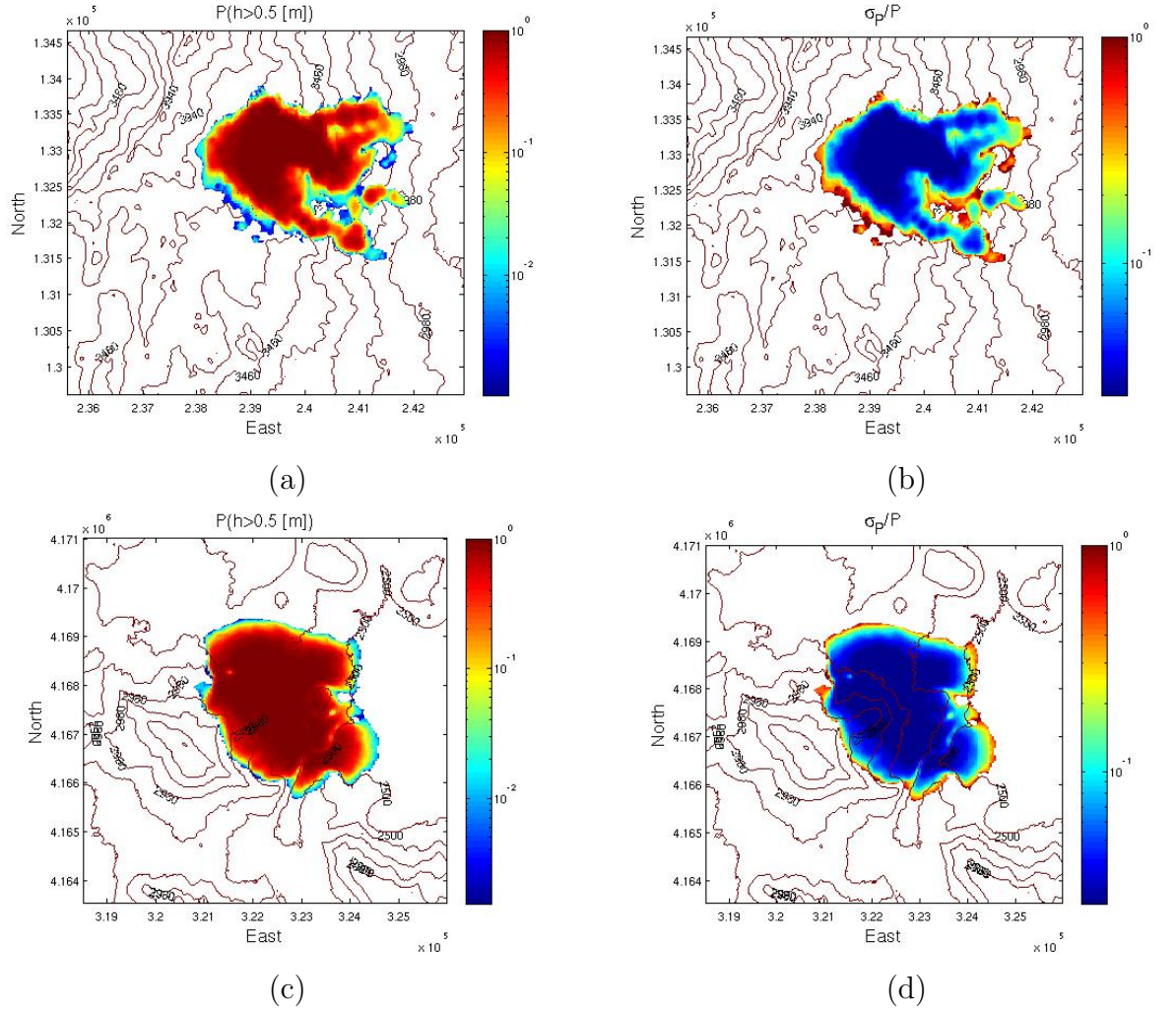
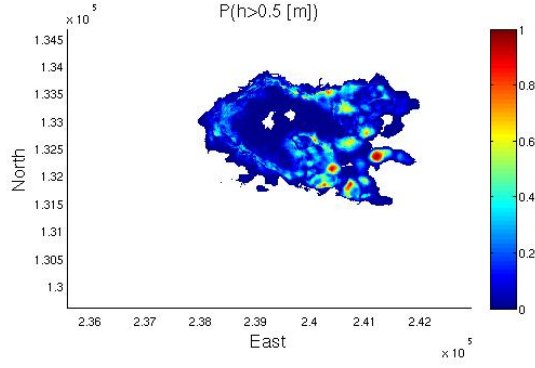
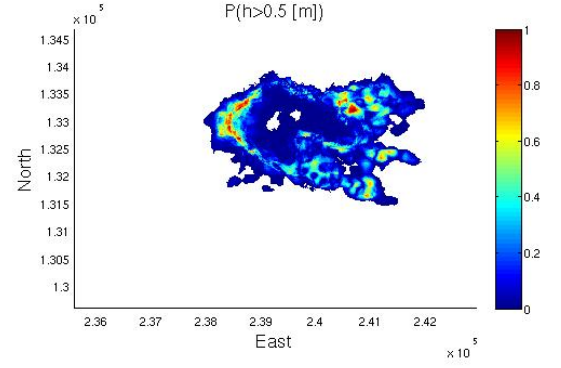


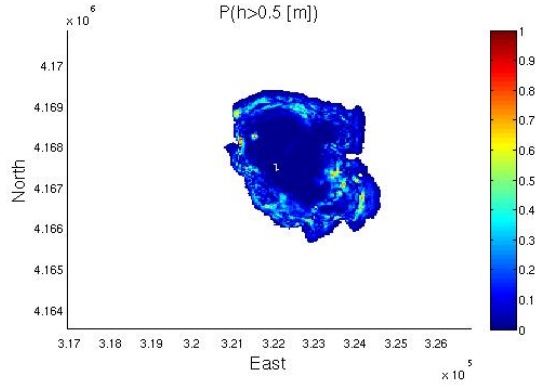
Figure 7: (a) The probability that flow will exceed 0.5 m for Galeras ASTER (b) Standard deviation in the estimate that the flow will exceed 0.5 m in depth for Galeras ASTER (c) The probability that flow will exceed 0.5 m for Mammoth TOPSAR (d) Standard deviation in the estimate that the flow will exceed 0.5 m in depth for Mammoth TOPSAR



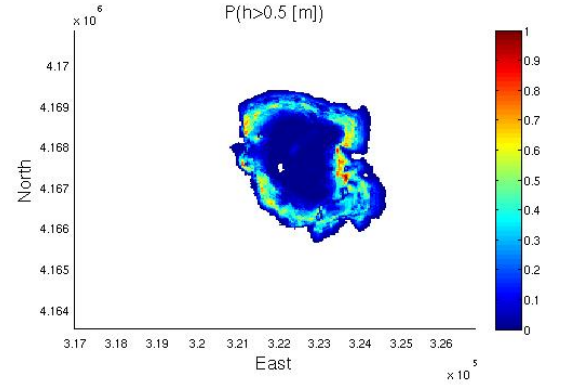
(a)



(b)

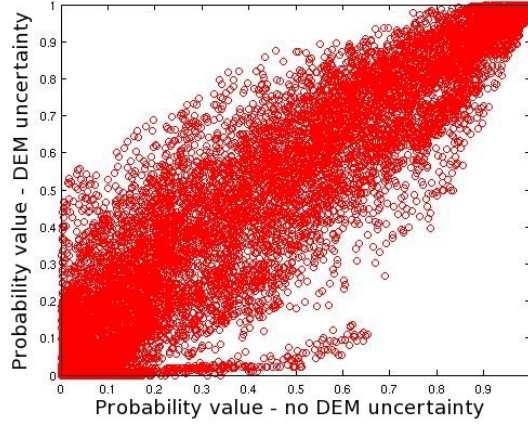


(c)

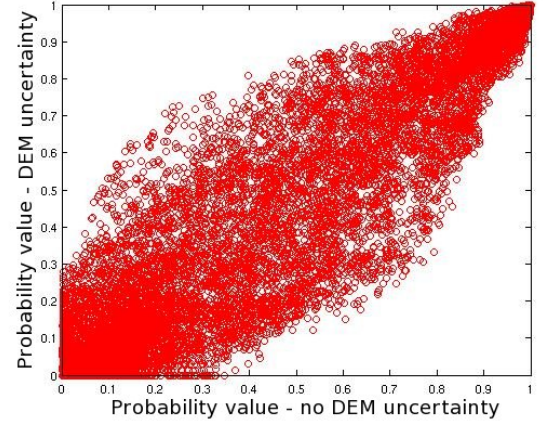


(d)

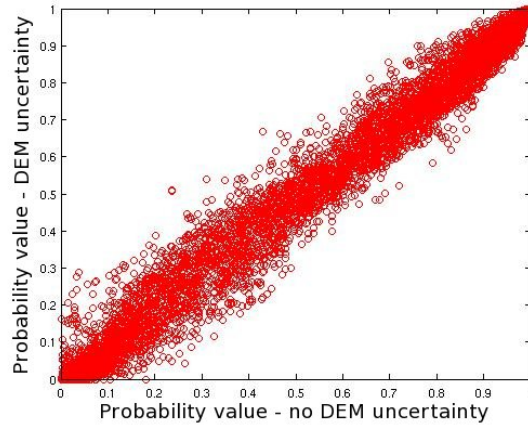
Figure 8: Probability difference map (absolute value) between: (a) Mammoth TOPSAR hazard map and the Method 1 hazard map (b) Mammoth TOPSAR hazard map and the Method 2 hazard map (c) Galeras ASTER hazard map and the Method 1 hazard map (d) Galeras ASTER hazard map and the Method 2 hazard map



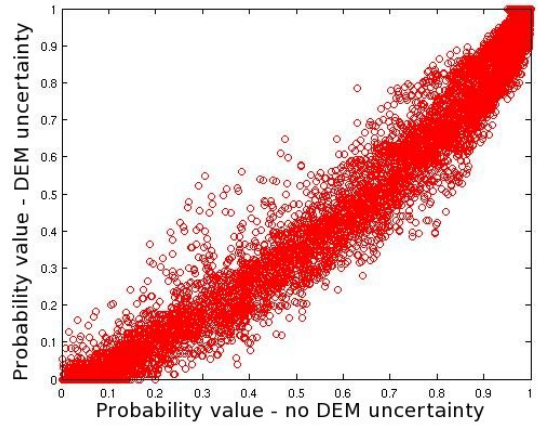
(a)



(b)



(c)



(d)

Figure 9: A comparison of the probability that flow will exceed 0.5 m when we don't assess for the uncertainty in the DEM and when we do, for: (a)Galeras ASTER no DEM uncertainty versus Galeras ASTER DEM uncertainty Method 1 (b)Galeras ASTER no DEM uncertainty versus Galeras ASTER DEM uncertainty Method 2 (c)Mammoth TOPSAR - no DEM uncertainty versus Mammoth TOPSAR - DEM uncertainty Method 1 (d)Mammoth TOPSAR - no DEM uncertainty versus Mammoth TOPSAR - DEM uncertainty Method 2